A Near-Field Quasi-Optical Measurement Technique for Probe-Fed High-Gain Backside-Radiating Antennas

van Rooijen, Nick; Spirito, M.; Triantafyllos, A. Bechrakis ; Llombart, N.; Alonso-delPino, M.

DOI
10.1109/IMS40175.2024.10600366

Publication date
2024

Document Version
Final published version

Published in
Proceedings of the 2024 IEEE/MTT-S International Microwave Symposium - IMS 2024

A Near-Field Quasi-Optical Measurement Technique for Probe-Fed High-Gain Backside-Radiating Antennas

Nick van Rooijen, M. Spirito, A. Bechrakis Triantafyllos, N. Llombart, M. Alonso-delPino
Delft University of Technology, The Netherlands
{n.vanrooijen, m.spirito, a.bechrakistriantafyllos, n.llombartjuan, m.alonsodelpino}@tudelft.nl

***Abstract*—This contribution presents the measurement strategy to accurately characterize probe-fed high-gain antennas operating in the sub-THz band. First, a near-field technique employing a quasi-optical system is introduced to enable characterization of backside radiating antennas (with respect to the landing pads). The proposed setup employs classical manipulators for probe landing (i.e., above the structure) and linear xyz CNC controlled translation stage. After, the calibration and modelling techniques to allow for an accurate input reflection-coefficient at the antenna input plane, and the estimation of the antenna gain, in a near field planar scanning system, are described in details. The experimental data of an high-gain backside-radiating lens antenna operating in D-band are presented to validate the proposed approach and characterization bench.**

***Keywords*—Near-field measurement technique, Probe-fed antenna, backside radiating antenna, antenna in-package characterization, sub-THz frequency characterization, D-band.**

I. Introduction

The sub-THz band >100GHz is being targeted for the upcoming 6th generation of communication systems, partially thanks to its large available bandwidth. High-capacity line-of-sight data links are being proposed for coverage in highly dense scenarios, such as the one presented in [1] or for back-haul systems [2]. For these scenarios, high-gain lens antennas are envisioned to realize the required transmit (Tx) and receiver (Rx) gain to establish the communication link [3].

However, the characterization complexity of these antennas increases exponentially when integrated in package or IC technology. In these cases, the Antenna Under Test (AUT) is a breakout of the final (fully integrated) system and is often probe fed to minimize the design of extra interfaces. In addition, given the high permittivity of the substrate materials used at these frequencies (i.e., silicon and III-V compounds) the radiation is in most cases realized through the substrate/package, resulting in feeding and radiation to be opposite to one another [3][4], [4]. In [5], various mm-wave probe-fed, backside-radiating, antenna characterization systems are reviewed, with several employing custom suspended probing environment and the use of complex multi-axis robotic arms to perform far-field measurements of the AUT. When high-gain lens antennas are considered, these approaches become impractical given the large volume of the setups for reaching the far-field distance. In [3], the mechanical restrictions lead to a phase-less spherical measurement system, which required multiple scans and iterative solver processes, contributing to a lower accuracy of the reconstructed phase.

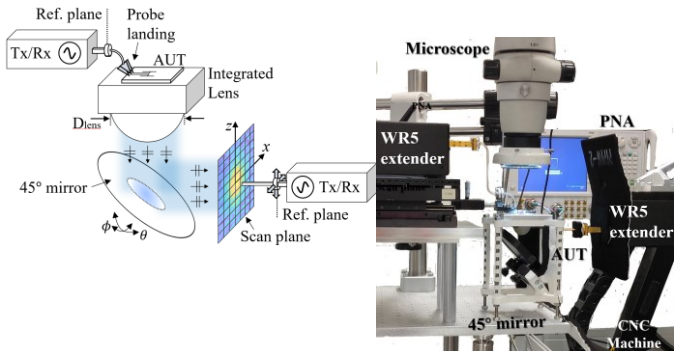

(a) (b)

Fig. 1. (a) Schematics and (b) photograph of the planar near-field antenna measurement setup.

The use of linear (motorized) translation stages, which enable high precision control even with higher loads compared to the robotic arms, can lead to an accurate phase acquisition in the sub-terahertz by employing mm-wave extenders based architectures. In this contribution, we propose the use of planar scanning systems in combination with quasi-optical (QO) approaches to characterize probe-fed and backside radiating antennas in the near-field. In [4], QO approaches have been employed for backside radiating antennas. Nevertheless, this far-field approach was hampered by strong vibrational coupling between the motorized stage and the RF landing-probe.

We present a novel approach using a 45° mirror providing a 90° rotation between the AUT radiation and the measurement plane, allowing to decouple the landing environment from the motorized one (see Fig. 1). Moreover, we detail the techniques to accurately characterize, in the sub-THz range, the antenna input impedance and the antenna gain in setups operating in the near field. To have an accurate reflection coefficient measurement, a calibration and modelling technique has been implemented to transfer the calibration accuracy of a two-port TRL to a one-port SOL, this is described in Section III. A technique to estimate the antenna directly from one set of measurements and simulations of the AUT in the near field, is introduced Section IV.

The proposed setup and the discussed techniques are validated on a probe-fed backside radiating lens antenna from [7]. The lens radiates a collimated beam of 30-32dBi of directivity across the 140-170GHz band.

2024 IEEE/MTT-S International Microwave Symposium - IMS 2024 | 979-8-3503-7504-6/24/$31.00 ©2024 IEEE | DOI: 10.1109/IMS40175.2024.10600366

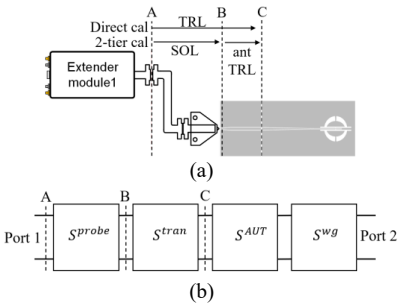

Fig. 2. (a) Schematic overview of the different calibration procedures to move the measurement plane from the waveguide flange A to the antenna reference plane C. (b) S-parameter boxes corresponding to the overview of (a).

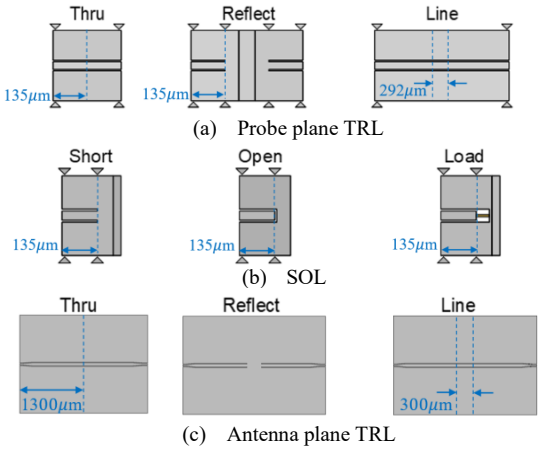

Fig. 3. (a) Probe-level TRL calibration. (b) 1-port SOL cal kit. (c) TRL cal kit for de-embedding until antenna reference plane (blue dashed lines). Images are not to scale.

II. Near Field Planar Antenna Measurement Setup

The near-field antenna measurement setup is shown in Fig. 1. It uses a CNC mechanical x-y-z scanner and a vector network analyzer (VNA) with WR5.1 frequency extender modules. The AUT is fed by a wafer probe mounted on a commercial micro manipulator, securely mounted on an optical table. The CNC scanner is stationed on a second optical table, thus preventing vibrations generated by the CNC machine from impacting the stability of the RF landing probe.

To enable the quasi-optical plane translation, the AUT is fixed to a metallic fixture that positions the lens antenna facing downward. The fixture holds a 45° flat mirror used to forward the radiation towards the near-field x-z measurement plane (see Fig. 1). The mirror is mounted on a manual rotation stage that can adjust the tilt in θ and ϕ. These two degrees of freedom allow for the alignment of the aperture antenna with the waveguide probe. For example, with the employed lens AUT which radiates a collimated beam, the alignment is achieved by maximizing the flatness of the measured phase on the scan plane. A circular 3 inch (~76mm) mirror provides a projected ellipse of 76mm × 54mm which is significantly larger than the projected circular aperture of the lens ($D_l = 30mm$). Since the lens antenna radiates a collimated beam, the beam will not diverge significantly in the proximity of the lens. In this case the distance between the lens and the mirror was 24mm, and from the mirror to the measurement plane was 64mm.

The near-field measurement plane, indicated in Fig. 1, is scanned by an open-ended waveguide probe connected to the second VDI WR5.1 frequency extender. Absorbers were used around the waveguide area of the extender to minimize the multiple reflections in the setup.

III. Reflection Coefficient Characterization

The input reflection coefficient of the AUT is a parameter of key importance in the characterization of the antenna. Conventionally, when an over-the-air setup is considered (i.e., port 1 connected to a wafer probe and port 2 connected to the probe antenna), a one-port calibration is carried out at port 1 and an eventual de-embedding step is employed to reach the antenna reference plane. When operating at sub-THz frequencies, the error introduced by the inaccuracies of the standard definitions (both commercially available as well as custom designed/EM simulated) of the devices used in the calibration process, i.e., short, open and load, makes this approach not pursuable. Calibration algorithms such as the thru-reflect-line (TRL) requiring partial knowledge of the standards response [7] are the standard approach to correct VNA systematic errors, and to derive fixture and interconnection responses at sub-THz [8]. Such approaches (offline TRL calibration) can be used to derive the entire input section bend with probe and antenna feed transition (i.e., S^{probe} and S^{tran} in Fig. 2), by using dedicated calibration structures in a two-port probe station. Nevertheless, the connecting and reconnecting of mechanical (pre-characterized) parts in sub-THz setups, leads to poor overall accuracy, as shown in Fig. 5, dashed, where the resulting antenna reflection coefficient is shown. To improve the accuracy of the measured input impedance, we use transfer devices to replicate the accuracy of the TRL calibration to the one-port calibration [9].

This procedure is accomplished by first performing a probe-level TRL calibration using the device shown in Fig. 3a, fabricated on a fused-silica substrate. After employing this calibration, the response of the SOL transfer standards shown in Fig. 3b is acquired. These transfer standards can then be employed in the setup of Fig. 2 to derive (without removing any connection in the setup) the de-embedding data from the waveguide calibration up to the probe tip (i.e., S^{probe} matrix). Finally, a TRL kit to extract the response of the transition from the landing pads to the antenna feed-line is measured, as a second-tier TRL (with respect to the probe plane TRL of Fig. 3a), providing the S^{tran} matrix of Fig. 2.

The quality of the calibration transfer standards, employed in the one port antenna setup, can be evaluated by comparing, in the two port probe station environment, the input impedance of the (unterminated, port 2) line of the transition TRL kit (shown in Fig. 3c) using two methods:

1) A direct TRL calibration using the custom designed calkit shown in Fig. 3c. This represents the reference data.
2) A one port calibration using the calibration transfer standard obtained using the procedure described above, employing the S^{tran} matrix to de-embed the transition section.

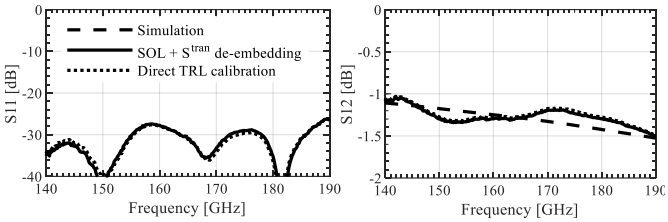

Fig. 4. (a) S_{11}^{DUT} and (c) S_{12}^{DUT} extracted from the direct calibration and from the used two-step calibration process.

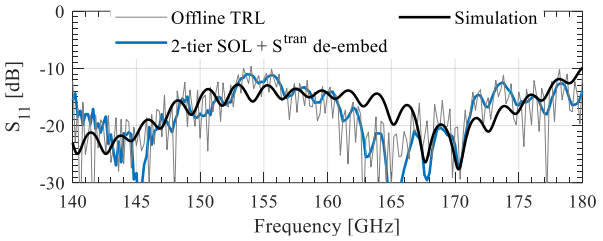

Fig. 5. Measured reflection coefficient of the AUT compared against full-wave simulations.

The results of this comparison are shown in Fig. 4, validating that the calibration transfer standards will achieve the same calibration quality as the one they have been derived from. applying the proposed approach to compute the input reflection coefficient of the antenna in the OTA setup, provides a significant reduction in the trace ripples, when comparing to the offline de-embedding approach, see solid blue trace in Fig. 5. Moreover, the figure shows good agreement with the CST full-wave simulated data, with only a shift in the main resonance peak which is attributed to small variations in the fabrication and assembly process.

IV. Gain Estimation in the Near-Field

Accurate calibration of absolute gain measurements proves to be a substantial challenge in near-field setups, particularly in the context of probe-fed antennas. First, a good phase stability is imperative to enable a near- to far-field transformation [6]. Furthermore, extracting the gain of the AUT using Friis transmission equation is not feasible in this scenario, as the power spreading does not follow the square of the distance.

In this contribution, instead of relating the power received of the AUT with a standard gain antenna as in [3,6], we propose to compare the power received of the AUT with the simulated or estimated value of this power received. For this, a good estimation of the power spread of the AUT can be obtained using semi-analytical methods.

The proposed strategy to extract the gain from the measured S-parameters relies on first extracting the far-field directivity D^{meas} via a near-field to far-field transformation. Second, the antenna loss L is estimated by comparing the measured transmission coefficient S_{21}^{smeas} with a simulated ideal transmission S_{21}^{sim} of the same AUT in a near-field known location. The required simulations steps will be explained in section B. Finally, the gain of the AUT will be derived from $G_{meas} = D_{meas} - L$, see section C.

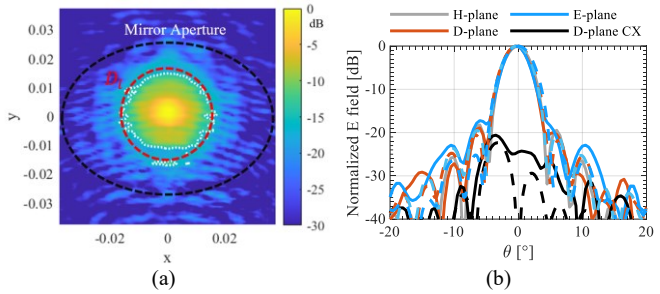

Fig. 6. (a) Measured electric field in the scan plane contoured with the -10dB field (dotted-white) and outlined the mirror aperture (dashed-black) and the lens aperture (dashed-red). (b) E/D/H-planes of the far-field radiation of the AUT after the NF-FF transformation. Dashed lines are simulated whereas solid is measured.

A. Radiation Pattern Measurements and Directivity

The near-field measurement plane, located at a distance of 8.8 cm from the tip of the lens, covered an area of 8 × 8 cm and was sampled with a step size of 0.88mm (corresponding to $\lambda_0/2$ at the maximum measurement frequency of 170 GHz). The electric field amplitude on the measurement plane at 155 GHz is shown in Fig. 6a. The lens aperture diameter, outline shown in red in Fig 6a, contains most of the field, the -10dB contour of the field is shown in white. The area between the lens aperture and the projection of the mirror, outlined in black, shows some (minor) diffraction effects probably due to the edges of the mirror.

Observing the far far-fields obtained after a near-field to far-field transformation in Fig. 6b, we note a good agreement with the simulations. The cross-polarized field was measured using a 90° waveguide twist and also presents an excellent agreement with the simulation (see trace D-plane CX).

The directivity of the extracted far-field patterns is shown in Fig. 7a, achieving an agreement within 1dB across the 140 - 170GHz band. This variation can be attributed to the truncation effect of the mirror and the near-field measurement plane.

B. Estimation of the power spreading in the near-field

As mentioned, to extract the gain, the measured transmission coefficient will be related to a simulation of the transmission of the lens AUT on the measurement plane. The simulated S_{21}^{sim} parameter can be expressed as

$$\left|S_{21}^{sim}\right|^2 = P_{Rx}/P_{acc}, \tag{1}$$

where P_{Rx} is the power received at the the waveguide probe tip and P_{acc} is the accepted power by the AUT, $P_{acc} = P_{tx}(1 - \left|S_{11}^{sim}\right|^2)$. The power received is calculated as

$$P_{Rx} = \Re\{S_z\}A_{eff}, \tag{2}$$

where $\vec{S}_z$ is the pointing vector, $\vec{S}_z = \frac{1}{2}\vec{E} \times \vec{H}^*$ at the measurement plane, in this case at 8.8 cm distance, and A_{eff} is the waveguide probe effective area, $A_{eff} = \frac{\lambda_0^2 G_{probe}}{4\pi}$. The gain G_{probe} was characterized through a far-field measurement. To

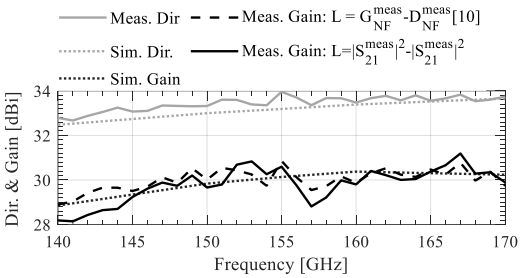

Fig. 7. Measured and simulated far-field directivity and gain of the AUT.

obtain $\vec{S}_z$, first a full-wave simulation of the antenna radiating in the lens medium is performed, without considering any ohmic or dielectric loss. After this simulation, the fields on the lens surface are approximated using physical optics, and are propagated to the scan plane of the same area and distance as the one measured.

C. Estimation of Losses and Extraction of the Gain

From the raw S-parameters obtained when the waveguide probe is aligned at the broadside position with the lens, the S_{21}^{meas} is obtained by de-embedding the transition until the antenna plane (Fig. 2). SOL calibration with S^{tran} de/embedding is performed to move the reference plane from the waveguide to the AUT (Fig. 2). The resulting S_{21}, after removing the reflection coefficients of the AUT and the waveguide probe, is expressed by $S_{21}^{meas} = S_{21}^{AUT}/(1 - |S_{11}^{AUT}|^2)$.

The resulting losses are then subtracted from the earlier measured directivity to arrive at the estimated antenna gain in Fig. 7. The measured gain is compared with the full-wave simulation, showing a good agreement within 1 dB in the 140-170GHz bandwidth. Note that the simulations do not include the effect of the reflection of the multiple antenna interfaces which may be the cause the rippling present in the directivity and the gain. This method is also compared with the estimation of the gain where loss is estimated from the subtraction of the measured near-field gain and directivity [10]. For very directive antennas with high front-to-back ratio as in this case, both measurements provide a good estimation of the antenna characteristics as shown in Fig 7. However, when the AUT suffers from strong back-side radiation and radiation towards large angles, the estimation of the near-field power spreading allows to understand and assess the radiation of the antenna in the measurement scan plane.

V. Conclusion

A measurement strategy to accurately characterize probe-fed high-gain antennas operating in the sub-THz band has been presented. Calibration and modelling techniques to transfer the calibration accuracy of a two-port TRL to a one-port SOL calibration were used. They enable an accurate input reflection coefficient measurement at the antenna input plane. The antenna gain was extracted directly from one set of measurements and one simulation. All these techniques have been corroborated with a set of measurements compared against simulations in the 140-170GHz band.

Acknowledgement

This work is supported by Huawei Technologies Sweden AB. The authors would like to thank Ulrik Imberg from Huawei for his assistance in this project.

References

[1] N. Llombart, D. Emer, M. A. Campo, and E. McCune, “Fly’s eye spherical antenna system for future Tbps wireless communications,” in The 11th European Conference on Antennas and Propagation (EuCAP 2017), (Paris, France), March. 2017.

[2] M. G. L. Frecassetti, J. F. Sevillano, D. del Río, M. I. Saglam, A. Lamminen and V. Ermolov, "D-Band Backhaul and Fronthaul Solutions for 5G Radio Access Network," 2022 52nd European Microwave Conference (EuMC), Milan, Italy, 2022, pp. 772-775

[3] A. Bisognin et al., "Ball Grid Array Module With Integrated Shaped Lens for 5G Backhaul/Fronthaul Communications in F-Band," in IEEE Transactions on Antennas and Propagation, vol. 65, no. 12, pp. 6380-6394, Dec. 2017, doi: 10.1109/TAP.2017.2755439.

[4] S. van Berkel et al., "Wideband Double Leaky Slot Lens Antennas in CMOS Technology at Submillimeter Wavelengths," in IEEE Transactions on Terahertz Science and Technology, vol. 10, no. 5, pp. 540-553, Sept. 2020, doi: 10.1109/TTHZ.2020.3006750.

[5] Z. Zheng, Y. Zhang, L. Shi, L. Wu and J. -F. Mao, "An Overview of Probe-Based Millimeter-Wave/Terahertz Far-Field Antenna Measurement Setups [Measurements Corner]," in IEEE Antennas and Propagation Magazine, vol. 63, no. 2, pp. 63-118, April 2021.

[6] IEEE Standard Test Procedures for Antennas, ANSI/IEEE Standard 149-1979, New York, NY, USA, 1979.

[7] G. F. Engen and C. A. Hoer, "Thru-reflect-line: An improved technique for calibrating the dual six-port automatic network analyzer", IEEE Trans. Microw. Theory Techn., vol. MTT-27, no. 12, pp. 987-993, Dec. 1979.

[8] D. F. Williams et al., “Calibration-Kit Design for Millimeter-Wave Silicon Integrated Circuits,” in IEEE Transactions on Microwave Theory and Techniques, vol. 61, no. 7, pp. 2685-2694, July 2013.

[9] S. Padmanabhan, L. Dunleavy, J. E. Daniel, A. Rodriguez and P. L. Kirby, "Broadband Space Conservative On-Wafer Network Analyzer Calibrations With More Complex Load and Thru Models," in IEEE Transactions on Microwave Theory and Techniques, vol. 54, no. 9, pp. 3583-3593, Sept. 2006.

[10] E. Gandini, A. Tamminen, A. Luukanen and N. Llombart, "Wide Field of View Inversely Magnified Dual-Lens for Near-Field Submillimeter Wavelength Imagers," in IEEE Transactions on Antennas and Propagation, vol. 66, no. 2, pp. 541-549, Feb. 2018.